

<https://doi.org/10.1038/s41524-024-01287-6>

Imaging and ferroelectric orientation mapping of photostriction in a single Bismuth Ferrite nanocrystal

Check for updates

Ahmed H. Mokhtar¹✉, David Serban¹, Daniel G. Porter², Gareth Nisbet², Steve Collins², Alessandro Bombardi² & Marcus C. Newton¹✉

The exploration of multiferroic materials and their interaction with light at the nanoscale presents a captivating frontier in materials science. Bismuth Ferrite (BiFeO₃, BFO), a standout among these materials, exhibits room-temperature ferroelectric and antiferromagnetic behaviour and magnetoelectric coupling. Of particular interest is the phenomenon of photostriction, the light-induced deformation of crystal structures, which enhances the prospect for device functionality based on these materials. Understanding and harnessing multiferroic phenomena holds significant promise in various technological applications, from optoelectronics to energy storage. The orientation of the ferroelectric axis is an important design parameter for devices formed from multiferroic materials. Determining its orientation in the laboratory frame of reference usually requires knowing multiple wavevector transfer (Q-Vector) directions, which can be challenging to establish due to the need for extensive reciprocal-space searches. Our study demonstrates a method to identify the ferroelectric axis orientation using Bragg Coherent X-ray Diffraction Imaging (BCDI) measurements at a single Q-vector direction. This method involves applying photostriction-inducing laser illumination across various laser polarisations. Our findings reveal that photostriction primarily occurs as a surface phenomenon at the nanoscale. Moreover, a photo-induced crystal length change ranging from 30 to 60 nm was observed, consistent with earlier findings on bulk material.

In the realm of materials science, the study of multiferroic materials, particularly their interaction with light at the nanoscale, has emerged as a captivating frontier^{1–3}. Multiferroics are characterised by their ability to exhibit multiple ferroic orders, such as ferromagnetism, ferroelectricity and ferroelasticity, within a single phase^{4–6}.

Amongst the interesting number of materials, Bismuth Ferrite (BiFeO₃, BFO) is particularly notable for its simultaneous ferroelectric and antiferromagnetic behaviour at room temperature, leading to robust magnetoelectric coupling^{7–10}.

BFO is a rhombohedral distorted perovskite unit cell with point group R3c, which can be described using a hexagonal frame of reference with lattice parameters $a_{\text{hex}} = 5.58 \text{ \AA}$ and $c_{\text{hex}} = 13.87 \text{ \AA}$ ^{11–13}. The ferroelectric polarisation emerges due to the displacement of Bi³⁺ ions from their centrosymmetric positions along the [001]_{hex} direction caused by the hybridisation between Bi³⁺ 6s and O²⁻ 2p orbitals⁷. This causes the formation of a local dipole moment and gives rise to a macroscopic spontaneous electric polarisation in the order of 100 $\mu\text{C}/\text{cm}^2$ ^{8,14}.

A phenomenon of significant interest in this context is photostriction – the light-induced deformation of crystal structures^{15–18}. BFO, with its perovskite metal-oxide composition and a relatively small 2.8 eV band-gap, is a prominent candidate for studying the interplay between light and material properties^{7,19–23}. Photostriction in BFO and similar ferroelectrics arises from the coupling of photovoltaic and inverse piezoelectric effects, offering a window into the nano-scale manipulation of material properties. The incident light generates electron-hole pairs, which are subsequently separated along the bulk electric field direction generated by the ferroelectric polarisation. In turn, this creates a depolarisation field screening effect, which gives rise to the inverse piezoelectric effect^{21,24–26}.

The magnitude of the effect is dependent on the wavelength, intensity and polarisation of the impinging light^{27–29}. Importantly, for the photostriction effect to be observed, the laser polarisation direction must align, at least partially, with the ferroelectric axis of the material¹⁹. The degree of photostriction is further enhanced when larger components of the laser polarisation are aligned along this ferroelectric axis, which is along the

¹School of Physics and Astronomy, University of Southampton. University Road, Southampton SO17 1BJ, UK. ²Beamline I16, Diamond Light Source. Harwell Science and Innovation Campus, Didcot, Oxfordshire OX11 0DE, UK. ✉e-mail: ahmm1g15@soton.ac.uk; m.c.newton@soton.ac.uk

(001)_{Hex} direction. This alignment-dependent response highlights the anisotropic nature of the photostriction effect in these materials.

The technological potential of photostriction in multiferroics like BFO includes applications in optoelectronics^{30–32}, energy storage^{33,34}, and advanced magnetoelectric memory devices^{35–38}. Determining the ferroelectric axis orientation accurately in the laboratory frame of reference is, therefore, crucial as it governs the materials' response to external stimuli and influences their practical device applications.

Bragg Coherent X-ray Diffraction Imaging (BCDI) is a powerful tool for unveiling the intricate dynamics of quantum materials at the nanoscale. BCDI allows for three-dimensional visualisation of crystal defects and is particularly adept at elucidating the intricate dynamics within these materials^{39–42}. The technique involves illuminating a sample with a spatially coherent X-ray beam such that the coherence length exceeds the dimensions of the crystal^{43,44}. Scattered light from the entire volume of the crystal interferes in the far field, producing a three-dimensional k-space diffraction pattern⁴⁵. The experiment collects the 2D diffraction pattern of a selected reflection onto a detector while the 3rd dimension is obtained by rocking the sample in increments and collecting the diffraction pattern at each step⁴⁰.

The Fourier space density and real space electron density are fundamentally related to each other via Fourier transforms^{46,47}, highlighting the necessity of phase information in BCDI experiments for accurately computing a sample's real space electron density⁴⁸. However, the experiment only measures the diffraction pattern intensity, rendering the direct extraction of phase information not possible and as a result, computational methods must be utilised to recover the phase^{49,50}. Iterative phase retrieval methods such as the Error Reduction^{51,52} and Hybrid Input-Output (HIO)^{53–55} and, more recently, deep learning algorithms based on Convolutional Neural Networks (CNNs)^{56–60} have proven effective to recover the complex three-dimensional electron density and phase information.

The recovered real space image reveals the crystal's morphology and atomic displacements from equilibrium positions projected onto the

Q-vector utilised in the experiment⁶¹. Specifically, the real space amplitude reveals the crystals' morphology while the atomic displacements are encoded in the phase information according to $\phi = \mathbf{Q} \cdot \mathbf{u}$, where \mathbf{u} is the displacement field, and ϕ denotes the phase information, thus offering a detailed understanding of the crystal structure and dynamics.

In the following, our study advances the understanding of the photostriction effect in a single nanocrystal by observing laser polarisation-dependent photostriction and quantitatively characterising its surface nature. We introduce a method to pinpoint the ferroelectric axis of a single multiferroic nanocrystal in the laboratory frame of reference using a single Q-vector directly from phase information. This technique is particularly valuable as BCDI evolves towards in-operando imaging of nanocrystals in devices, where knowing the crystal orientation is critical. Our approach significantly simplifies the otherwise daunting task of extensive reciprocal space exploration for a single nanocrystal. The integration of a rapid CNN deep learning algorithm with this finding enhances both the speed and accuracy of determining crystal orientation, representing an important development for future BCDI applications and device functionality characterisation.

Results

Bragg coherent diffraction imaging experiment

Nanocrystals of BFO were synthesised following the procedure detailed in the Methods section. The Bragg Coherent X-ray Diffraction Imaging (BCDI) experiments were conducted in air at the Diamond Light Source synchrotron facility on beamline I16, using 9 keV X-rays in Bragg geometry. This setup, illustrated in Fig. 1, was equipped with a 6-axis kappa diffractometer. The X-ray beam was focused to a size of 200 × 30 μm, using front slits of 20 × 20 μm. Through surface area

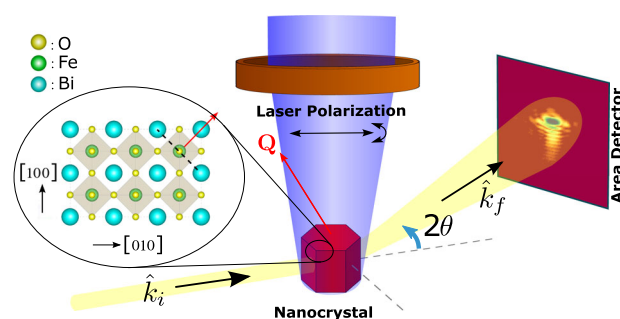


Fig. 1 | The experimental setup. An illustration of the experimental geometry in a Bragg CDI experiment. Crystal structure visualisation presented as an inset is prepared using the VESTA software⁶⁶.

scans, we identified and positioned a single BFO nanocrystal at the (110)_{Hex} specular reflection, which was aligned at the eucentric point of the diffractometer.

A 5 mW polarised 405 nm blue laser was directed onto the sample and focused at the eucentric point. Rocking curve measurements were then performed for the ground state crystal and under 5 different laser polarisation directions to obtain a series of 3D diffraction pattern data sets.

Deep learning phase retrieval

For phase retrieval, we utilised a deep learning model based on a CNN architecture⁵⁶ for its improved robustness and efficiency over traditional iterative phase retrieval techniques, which are prone to stagnation problems leading to missing density or pebbling effects in the reconstructed density. The enhanced robustness ensures a more complete and faithful reconstruction of the object, mitigating common issues associated with iterative approaches.

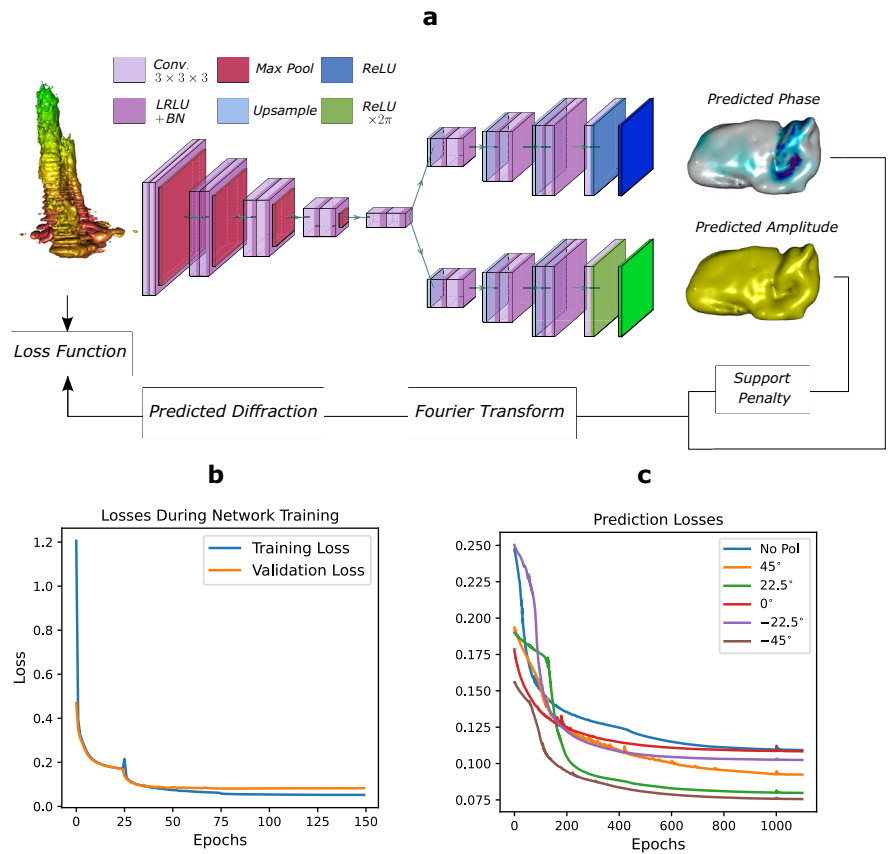
Figure 2a presents the CNN used, which operates on an encoder-decoder framework, wherein the measured diffraction amplitude is first encoded into a feature space, then split into two branches for independent amplitude and phase recovery. The procedure of our network's training is elaborated in the Methods section, while the training and validation losses are depicted in Fig. 2b.

The simulated data set, designed for the initial training phase of our CNN, comprises idealised Fourier transform pairs⁵⁶. These pairs consist of two main components: the real space representation, characterised by perfectly hexagonal objects with uniform dimensions and a Gaussian-correlated phase profile, and their corresponding Fourier transform, which represents the ideal simulated diffraction patterns. In contrast, the experimental data sourced from synchrotron facilities includes deviations from these ideal conditions, encompassing noise and variations in object dimensions and phase profiles and lacks a predefined 'ground truth' for the real space image.

Therefore, our prediction methodology incorporated a reconstruction refinement step, paralleling a transfer learning mechanism, where the pre-trained neural network initiated the reconstruction process. We processed the experimental diffraction patterns through the network for hundreds of epochs, continuously adjusting the network's parameters based on computed losses and penalty terms. This strategy offered refined fine-tuning for reconstructions, enhancing the robustness and specificity of the model to our datasets.

Furthermore, we integrated a real-space support penalty to guide the algorithm more effectively toward adhering to the system's known dynamics and constraints. In iterative phase retrieval algorithms, the support serves as a constraint, selectively adjusting or discarding amplitudes outside a predefined spatial region to enhance phase recovery^{62,63}. In contrast, in our framework, this concept is re-imagined as a penalty mechanism that penalises the network during the refinement phase for generating amplitude outside the defined support, thereby training the network to minimise loss by adhering closely to the crystal morphology. This

Fig. 2 | Phase retrieval method. **a** A block diagram representation of the CNN during the prediction phase. During the training step, the support penalty is replaced with the ground truth loss for the amplitude and phase. In the encoder branch, the size of the array is halved at every step using Max Pool operations and the depth of the feature map is doubled using a convolution layer. The initial layer expands the number of channels by 64. In the decoder branches, the size is doubled using an upsampling method and the depth is halved at each step using a deconvolution layer. The size of the output array is made to be half the size of the input diffraction pattern. We used a Leaky RELU activation function for all the layers except for the last layer, where a RELU function is used instead. **b** The loss diagram during the training and validation of the model. **c** The loss during the prediction of the final reconstruction for each laser polarisation.



translation of a classical phase retrieval technique into a modern deep learning setting leverages the strengths of both methods and also provides a pathway to improve algorithmic performance and fidelity in the CNN framework.

This penalty bridges the different conditions during training and prediction, adapting the CNN trained on idealised data for application to the more complex and variable experimental data. It compensates for the absence of real-space ground truth in experimental measurements, enabling the network to make informed predictions about real-space information.

This penalty was added to the real space amplitude’s loss term when predictions fell outside a predefined support region, thus ensuring fidelity to the system’s constraints. The penalty-augmented loss function derived from ref. 56 is formulated in Eq. (2c), with the addition of ζ which represents the penalty function, defined in Eq. (3) and S denotes the support; I_p and I_g represent the predicted and ground truth Fourier space intensities, respectively, and L_1 is the normalised mean-squared error, Eq. (2).

$$L_{Predict} = \frac{1}{\alpha_1 + \alpha_2} [\alpha_1 L_1 (\sqrt{I_p(\mathbf{q})}, \sqrt{I_g(\mathbf{q})}) + \alpha_2 \zeta(\rho(\mathbf{r}), S)] \quad (1)$$

$$L_1 = \frac{\sum_{\mathbf{q}} |I_p(\mathbf{q}) - I_g(\mathbf{q})|^2}{\sum_{\mathbf{q}} I_g(\mathbf{q})^2} \quad (2)$$

$$\zeta(\rho(\mathbf{r}), S) = \frac{\sum_{\mathbf{r} \notin S} \rho(\mathbf{r})}{\sum_{\mathbf{r}} \rho(\mathbf{r})} \quad (3)$$

The support region is defined in an iterative process, starting with a model prediction with a loose predefined support determined from the diffraction patterns’ autocorrelation function to identify the crystal’s general shape initially.

Subsequently, a tight support is crafted around the identified object using a shrink wrap method, effectively excluding any noise-induced amplitudes.

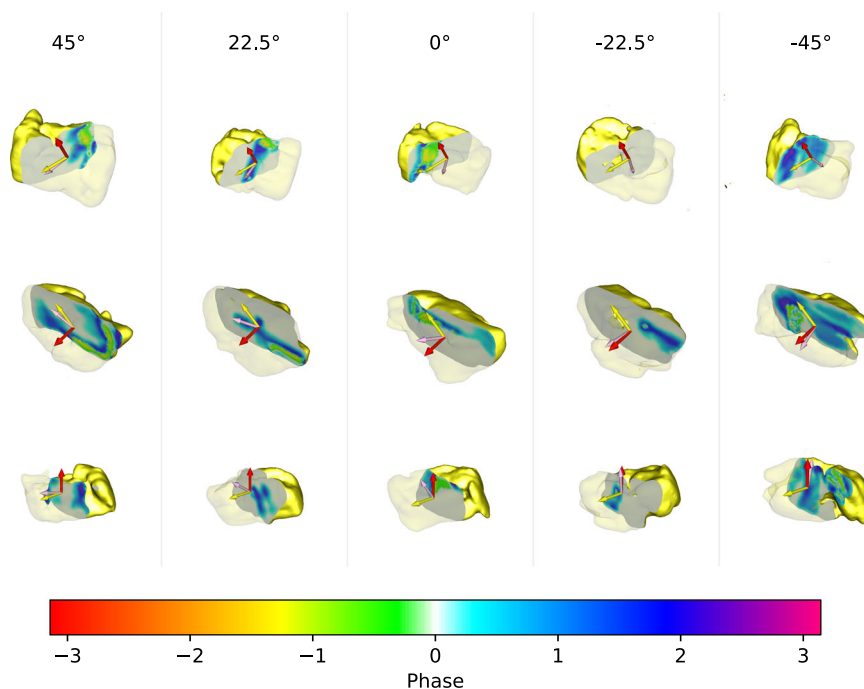
Including this penalty term significantly enhanced the algorithm’s capability to produce precise and consistent reconstructions for complex datasets as is depicted in Supplementary Fig. 5, making it an invaluable asset in phase retrieval. This approach’s flexibility allows for its extension to phase penalties, aligning the reconstructions more closely with known system dynamics. Since all diffraction patterns originated from the same crystal structure, we employed a consistent support region across all datasets. This provided a uniform framework for analysis. The model was then used to reconstruct the diffraction patterns for 1100 epochs using the ADAM optimiser⁶⁴, consistently producing low loss across all five data sets, underscoring its robustness and adaptability to complex crystallographic data.

The recovered 3D images demonstrated good convergence, consistent amplitude profiles, and reproducible phases. The phase retrieval transfer function (PRTF) computed for each of the reconstructed images demonstrated good resolution, Supplementary Fig. 1. Fig. 2c highlights the low losses achieved using this method, demonstrating a close match between the original diffraction pattern and the Fourier transform of the predicted objects. Detailed χ^2 losses for each data set are presented in Supplementary Table 1.

Ferroelectric axis orientation determination

The 3D images were then subjected to a coordinate transformation into the laboratory frame of refs. 45,65. From this, the nominal size of the crystal was determined to be $960 \times 660 \times 990 \text{ nm}^3$ with a spatial resolution of 15 nm. The recovered phase information, ranging from $-\pi$ to π , signifies atomic displacements relative to equilibrium positions along the \mathbf{Q} -vector direction. A phase of π indicates a displacement of one unit cell in the direction of the \mathbf{Q} -vector, whereas $-\pi$ represents an equivalent

Fig. 3 | Three-dimensional crystal rendering. The phase in the reconstructed crystals ranging from $-\pi$ to π represented through a colour map projected onto the amplitude image. Cross-sectional slices were taken through the centre of the crystal in three different orientations for each laser polarisation. Each column corresponds to the crystal under the influence of varying laser polarisations illustrating variations in the recovered phase information which is representative of the photo-induced lattice distortions. Each row showcases different cross-sectional planes within the crystal to offer a comprehensive 3D perspective of the internal structure. The 3 vectors rendered on the surface represent the Q-vector (red), the determined optimal ferroelectric axis (yellow) and the laser polarisation direction (purple).



displacement in the direction opposite to \mathbf{Q} . This interpretation of phase values allows for a detailed mapping of lattice distortions along the Q-vector direction, which is visualised as a colour map projected onto the amplitude in Fig. 3 for cross-sectional planes through the centre of the crystal.

From the experimental geometry, the direction of the Q-vector of the BCDI experiment was determined relative to the reconstructed crystal, specifically in the lab frame. In addition, the directions of the laser polarisations, \mathbf{L} , were determined in conjunction with the Q-vector direction calculations for each of the five data sets, as shown in Fig. 3.

The orientation of the ferroelectric axis within the crystal is determined based on the understanding that incident laser light induces electron-hole pair generation within BFO. These pairs are subsequently separated along the direction of the internal electric field, a consequence of the ferroelectric polarisation inherent to BFO. This separation effect leads to the establishment of a depolarisation field, which, in turn, triggers the inverse piezoelectric effect. The core of our analysis lies in identifying the direction along which the maximum structural deformation occurs. This is directly influenced by the direction of the ferroelectric polarisation, as the induced depolarisation fields are aligned accordingly. By analysing the directional phase variation, we can pinpoint the direction showcasing the greatest phase change, which we interpret as the ferroelectric axis of the material.

A critical step in our analysis was defining the set of all possible vectors for the known $(001)_{\text{Hex}}$ ferroelectric axis direction \mathbf{F} in the laboratory frame of reference, using the experimental geometry constraints. This involved calculating the angle between the $(110)_{\text{Hex}}$ reciprocal space vector, which aligns with the experiment's Q-vector, and the $(001)_{\text{Hex}}$ vector direction which aligns with the material's ferroelectric axis. This calculation, based on lattice parameters and crystal properties, was pivotal for establishing the set of all possible vectors for the $(001)_{\text{Hex}}$ ferroelectric axis, oriented around the Q-vector. This angle computation provided a fundamental boundary condition, guiding our interpretation of phase variations in relation to laser polarisation and ferroelectric axis alignment.

Using an optimisation approach, we determined the optimal direction of the ferroelectric axis, \mathbf{F}^* , within the set of geometrically possible vectors. This involved calculating the relative phase difference

$(\delta\phi_n = \phi_n - \phi_0)$, where ϕ_0 represents the ground state phase information with no laser illumination, and ϕ_n is the phase information under different laser polarisation conditions. This step, aimed at isolating the phase variation due to photostriction, helped minimise the influence of crystal imperfections. We employed a metric, the root sum square of the phase directional derivative (denoted as Ω and defined in Eq. (4)), to quantify the degree of phase variation along a particular direction. We applied this metric for the set of all feasible ferroelectric axis directions across all the reconstructed phase information data sets ($\delta\phi_n$) to identify the direction that maximises Ω .

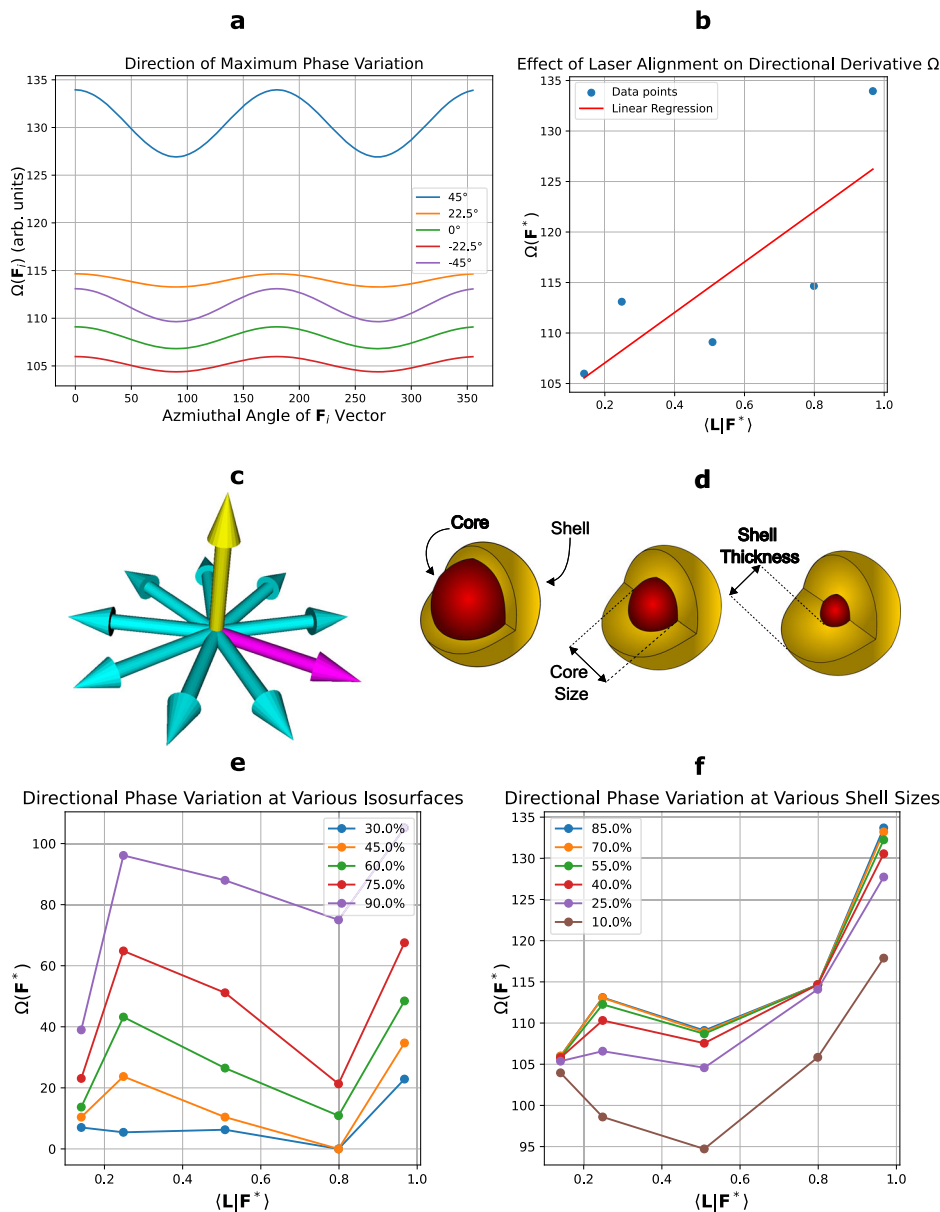
$$\Omega(\mathbf{F}) = \sqrt{\sum_{i=x,y,z} \left(\frac{d(\delta\phi)}{dr_i} \times \mathbf{F}_i \right)^2} \quad (4)$$

$$\mathbf{F}^* = \arg \max_{\mathbf{F}} \Omega(\mathbf{F}) \quad (5)$$

Figure 4 visually illustrates our analysis, displaying a uniform pattern across all data sets, with different magnitudes. This consistency in direction across the various sets emphasizes the strength and dependability of our method in identifying the ferroelectric axis. Notably, two peaks are observed at exactly the same positions, separated by an angle of 180° . Such symmetry indicates flexibility in choosing the direction of the ferroelectric axis, either positive or negative, without affecting the overall analysis. In our study, one of these maxima was selected, and the corresponding vector from the set of all possible ferroelectric vectors was determined to be the optimal vector \mathbf{F}^* . The primary objective of our study is to ascertain the ferroelectric axis, with the polarity of direction being a secondary consideration that does not impact the findings.

We determined the relationship between the phase variation metric Ω along the determined ferroelectric axis direction \mathbf{F}^* and the alignment of laser polarisation with the ferroelectric axis. We quantified the alignment between each individual laser polarisation direction and the determined ferroelectric axis direction using an inner product calculation, $\langle \mathbf{L} | \mathbf{F}^* \rangle$. Using the data available, we observed a linear relationship, confirmed by fitting a linear regression line (Fig. 4b) with a mean squared error that was calculated to be 0.047, confirming the good alignment. This indicates a proportional increase in phase

Fig. 4 | Phase variation analysis. **a** The relationship between the directional phase variation metric Ω and the azimuthal angle of the ferroelectric vector around the \mathbf{Q} from the set of all possible vectors for all the data sets. The maximum of which corresponds to the direction of the optimal ferroelectric axis. **c** An illustration of the \mathbf{Q} -Vector (yellow) and the set of possible ferroelectric vectors (cyan) with the optimal vector highlighted (purple). **b** A plot of the directional phase variation metric Ω along the determined ferroelectric axis \mathbf{F}^* showing its relationship with the projection of the laser polarisation along the \mathbf{F}^* expressed as an inner product $(\mathbf{L}|\mathbf{F}^*)$. A linear regression was also fitted to confirm the relationship. **d** A visualisation of the core sizes and shell thicknesses. **e** Determining the directional phase variation behaviour at the core of the crystal for different sized cores and (**f**) at the surface with different thicknesses of the shell.



variation as the laser polarisation aligns more closely with the ferroelectric axis, thus highlighting the connection between laser polarisation alignment and photo-induced strain.

Photostriction’s impact on the crystal’s dimensions was also evident in our findings through analysis of the reconstructed crystal amplitude. We observed a modest increase in crystal length along the ferroelectric axis between the ground state and the dataset with maximum laser polarisation alignment. The measured length change, within the spatial resolution of the reconstruction, was found to be 30–60 nm, which is in good agreement with previous studies conducted on a macroscopic crystal¹⁹.

Volume uniformity of photostriction determination

To discern whether the observed photostriction effect primarily originates at the crystal’s surface or within its bulk, we examined the core of the crystal, progressively including a higher percentage of the crystal’s amplitude, ranging from 30% to 90%. Our analysis, detailed in Fig. 4e, shows a noticeable decline in the effect’s magnitude on smaller isosurfaces. As more of the crystal was included, we observed a non-

constant effect, although its magnitude did not match that of the full crystal.

Conversely, the effect was investigated at the surface for varying shell thicknesses ranging from 10% to 85% of the crystal amplitude’s density. As shown in Fig. 4f, even at a minimal 10% shell thickness, the effect was non-linear and with a magnitude comparable to that of the full crystal. This effect became increasingly evident at a shell thickness of 25%, albeit with a slightly reduced effect magnitude. Further inclusions of the crystal in the analysis yielded only marginal increases to the effect. These patterns strongly suggest that the photostriction predominately occurs with the outer 25% of the crystal in a shell of approximately 120 nm thickness. The surface-dominated effect is consistent with other findings²⁸.

Discussion

In this study, we have imaged a single BFO nanocrystal using Bragg Coherent X-ray Diffraction Imaging (BCDI) while varying laser polarisation directions to observe the photostriction effect. Our experimental design, combined with a deep learning approach,

facilitated the successful generation of 3D real-space images of our series of diffraction patterns. This was achieved by integrating a support constraint into the CNN as a penalty term on reconstructed amplitude, resulting in high-quality image reconstruction.

Moreover, we introduced a method to determine the orientation of the ferroelectric axis in three dimensions using a single \mathbf{Q} -vector. By employing an optimisation approach, we identified the principal axis of phase variation across all data sets from the set of geometrically possible directions for the ferroelectric axis. Notably, we observed directional coherence between the datasets, as they all indicated the same directions, thus underscoring the reliability of our method. This methodology enabled us to accurately determine the ferroelectric axis orientation in a single multiferroic nanocrystal subjected to polarised laser illumination, utilising only the \mathbf{Q} -vector and recovered phase information.

In addition, our results also revealed a photostriction-induced change in the length of the crystal by 30–60 nm, in agreement with previous findings performed on bulk material. This consistency further validates our experimental approach. Significantly, we confirmed that the photostriction effect predominantly manifests as a surface phenomenon occurring within a thickness of approximately 120 nm.

The implications of our research are far-reaching, offering valuable insights that could significantly advance the development of materials and technologies. Therefore, this work lays the groundwork for the non-contact characterisation of integrated multiferroic devices, providing a vital tool for scientists and engineers.

Methods

Synthesis of BiFeO₃ nanocrystals

Nanocrystals of BiFeO₃ were synthesised using a bottom-up epitaxial method on a Sapphire R-plane substrate using pulsed laser deposition (PLD). A 248 nm, 20 mJ KrF excimer laser was used to ablate a solid target of BiFeO₃ at a temperature of 700 °C in vacuum conditions of 10⁻⁴ mbar and Oxygen partial pressure. An initial slow deposition cycle with short laser cycles is performed to seed the nanocrystal growth which is left to anneal for a few hours. Subsequent faster laser cycles at slightly higher temperature ensures the ablated material condenses at the seed sites. X-ray diffraction measurements confirm a single-phase BiFeO₃ growth. The particles' size formed a uniform distribution in the 500–1500 nm range.

Training of convolutional neural network

Simulated Fourier pairs are used during the network training process, wherein the Fourier space objects are forwarded through the network to generate phase and amplitude predictions, which are subsequently compared to ground truth objects using a loss function, L , as in Eq. (6). Here, L_1 and L_2 represent losses for real space amplitude and phase, respectively. Additionally, L_3 leverages Fourier transforms of predictions to compute losses relative to the square root of input intensities, where the relative weights of these functions are determined by integer parameters α_1 , α_2 , and α_3 . Back-propagation and training spanned 150 epochs using 30,000 Fourier pairs which achieved low and consistent loss profile while employing the ADAM optimiser.

$$L_{\text{Train}} = \frac{1}{\alpha_1 + \alpha_2 + \alpha_3} \left[\alpha_1 L_1(A_p, A_g) + \alpha_2 L_2(\phi_p, \phi_g) + \alpha_3 L_3(\sqrt{I_p}, \sqrt{I_g}) \right] \quad (6)$$

Data availability

The data underpinning the findings of this study are available from M.C.N. upon reasonable request.

Code availability

The code utilised in this study are available from M.C.N. upon reasonable request.

Received: 16 January 2024; Accepted: 24 April 2024;

Published online: 07 May 2024

References

- Spaldin, N. Multiferroics beyond electric-field control of magnetism. *Proc. R. Soc. A* **476**, 20190542 (2020).
- Spaldin, N. & Ramesh, R. Advances in magnetoelectric multiferroics. *Nat. Mater.* **18**, 203–212 (2019).
- Hur, N. et al. Electric polarization reversal and memory in a multiferroic material induced by magnetic fields. *Nature* **429**, 392–395 (2004).
- Ramesh, R. & Spaldin, N. Multiferroics: progress and prospects in thin films. *Nat. Mater.* **6**, 21–29 (2007).
- Hill, N. Why Are There so Few Magnetic Ferroelectrics? *J. Phys. Chem. B* **104**, 6694–6709 (2000).
- Cheong, S. & Mostovoy, M. Multiferroics: a magnetic twist for ferroelectricity. *Nat. Mater.* **6**, 13–20 (2007).
- Wang, J. Epitaxial BiFeO₃ Multiferroic Thin Film Heterostructures. *Science* **299**, 1719–1722 (2003).
- Lebeugle, D. Room-temperature coexistence of large electric polarization and magnetic order in BiFeO₃ single crystals. *Phys. Rev. B* **76**, 024116 (2007).
- Choi, T., Lee, S., Choi, Y., Kiryukhin, V. & Cheong, S. Switchable Ferroelectric Diode and Photovoltaic Effect in BiFeO₃. *Science* **324**, 63–66 (2009).
- Wang, N. Structure, Performance, and Application of BiFeO₃ Nanomaterials. *Nano Micro Lett.* **12**, 81 (2020).
- Kubel, F. & Schmid, H. Structure of a ferroelectric and ferroelastic monodomain crystal of the perovskite BiFeO₃. *Acta Crystallogr. Sect. B: Struct. Sci.* **46**, 698–702 (1990).
- Moreau, J., Michel, C., Gerson, R. & James, W. Ferroelectric BiFeO₃ X-ray and neutron diffraction study. *J. Phys. Chem. Solids* **32**, 1315–1320 (1971).
- Bucci, J., Robertson, B. & James, W. The precision determination of the lattice parameters and the coefficients of thermal expansion of BiFeO₃. *J. Appl. Crystallogr.* **5**, 187–191 (1972).
- Shvartsman, V., Kleemann, W., Haumont, R. & Kreisel, J. Large bulk polarization and regular domain structure in ceramic BiFeO₃. *Appl. Phys. Lett.* **90**, 172115 (2007).
- Figielski, T. Photostriction Effect in Germanium. *Phys. Status Solidi B* **1**, 306–316 (1961).
- Lagowski, J. & Gatos, H. Photomechanical Effect in Noncentrosymmetric Semiconductors-CdS. *Appl. Phys. Lett.* **20**, 14–16 (1972).
- Łagowski, J. & Gatos, H. Photomechanical vibration of thin crystals of polar semiconductors. *Surf. Sci.* **45**, 353–370 (1974).
- Tatsuzaki, I., Itoh, K., Ueda, S. & Shindo, Y. Strain Along c Axis of SbSI Caused by Illumination in dc Electric Field. *Phys. Rev. Lett.* **17**, 198–200 (1966).
- Kundys, B., Viret, M., Colson, D. & Kundys, D. Light-induced size changes in BiFeO₃ crystals. *Nat. Mater.* **9**, 803–805 (2010).
- Lejman, M. et al. Giant ultrafast photo-induced shear strain in ferroelectric BiFeO₃. *Nat. Commun.* **5**, pp. (2014).
- Schick, D. et al. Localized excited charge carriers generate ultrafast inhomogeneous strain in the multiferroic BiFeO₃. *Phys. Rev. Lett.* **112**, 097602 (2014).
- Catalan, G. & Scott, J. Physics and Applications of Bismuth Ferrite. *Adv. Mater.* **21**, 2463–2485 (2009).
- Kundys, B. Photostrictive materials. *Appl. Phys. Rev.* **2**, 011301 (2015).
- Wen, H. et al. Electronic Origin of Ultrafast Photoinduced Strain in BiFeO₃. *Phys. Rev. Lett.* **110**, 037601 (2013).
- Li, Y. et al. Nanoscale excitonic photovoltaic mechanism in ferroelectric BiFeO₃ thin films. *APL Mater.* **6**, 084905 (2018).

26. Chen, C. & Yi, Z. Photostrictive Effect: Characterization Techniques, Materials, and Applications. *Adv. Funct. Mater.* **31**, 2010706 (2021).
27. Kundys, B. et al. Wavelength dependence of photoinduced deformation in BiFeO₃. *Phys. Rev. B* **85**, 092301 (2012).
28. Newton, M., Parsons, A., Wagner, U. & Rau, C. Coherent x-ray diffraction imaging of photo-induced structural changes in BiFeO₃ nanocrystals. *N. J. Phys.* **18**, 093003 (2016).
29. Yang, Y., Paillard, C., Xu, B. & Bellaiche, L. Photostriction and elasto-optic response in multiferroics and ferroelectrics from first principles. *J. Phys. Condens. Matter* **30**, 073001 (2018).
30. Sando, D. et al. Large elasto-optic effect and reversible electrochromism in multiferroic BiFeO₃. *Nat. Commun.* **7**, 10718 (2016).
31. Liou, Y. et al. Deterministic optical control of room temperature multiferroicity in BiFeO₃ thin films. *Nat. Mat.* **18**, 580–587 (2019).
32. Jin, Z. et al. Strain modulated transient photostriction in La and Nb codoped multiferroic BiFeO₃ thin films. *Appl. Phys. Lett.* **101**, 242902 (2012).
33. Zhu, L. et al. Phase structure and energy storage performance for BiFeO₃-BaTiO₃ based lead-free ferroelectric ceramics. *Ceram. Int.* **45**, 20266–20275 (2019).
34. Yu, Z. et al. Microstructure effects on the energy storage density in BiFeO₃-based ferroelectric ceramics. *Ceram. Int.* **47**, 12735–12741 (2021).
35. Sharma, P. et al. Nonvolatile ferroelectric domain wall memory. *Sci. Adv.* **3**, e1700512 (2017).
36. Li, Z. et al. High-density array of ferroelectric nanodots with robust and reversibly switchable topological domain states. *Sci. Adv.* **3**, e1700919 (2017).
37. Wang, H. et al. Direct observation of room-temperature out-of-plane ferroelectricity and tunneling electroresistance at the two-dimensional limit. *Nat. Commun.* **9**, 3319 (2018).
38. Bibes, M. & Barthélémy, A. Towards a magnetoelectric memory. *Nat. Mat.* **7**, 425–426 (2008).
39. Miao, J., Ishikawa, T., Robinson, I. & Murnane, M. Beyond crystallography: Diffractive imaging using coherent x-ray light sources. *Science* **348**, 530–535 (2015).
40. Williams, G., Pfeifer, M., Vartanyants, I. & Robinson, I. Three-Dimensional Imaging of Microstructure in Au Nanocrystals. *Phys. Rev. Lett.* **90**, 175501 (2003).
41. Newton, M., Leake, S., Harder, R. & Robinson, I. Three-dimensional imaging of strain in a single ZnO nanorod. *Nat. Mat.* **9**, 120–124 (2010).
42. Pfeifer, M., Williams, G., Vartanyants, I., Harder, R. & Robinson, I. Three-dimensional mapping of a deformation field inside a nanocrystal. *Nature* **442**, 63–66 (2006).
43. Robinson, I. & Harder, R. Coherent X-ray diffraction imaging of strain at the nanoscale. *Nat. Mat.* **8**, 291–298 (2009).
44. Clark, J., Huang, X., Harder, R. & Robinson, I. High-resolution three-dimensional partially coherent diffraction imaging. *Nat. Commun.* **3**, 993 (2012).
45. Mokhtar, A., Serban, D. & Newton, M. Simulation of Bragg coherent diffraction imaging. *J. Phys. Commun.* **6**, 055003 (2022).
46. Miao, J., Sayre, D. & Chapman, H. Phase retrieval from the magnitude of the Fourier transforms of nonperiodic objects. *J. Opt. Soc. Am. A* **15**, 1662–1669 (1998).
47. Fienup, J. Reconstruction of an object from the modulus of its Fourier transform. *Opt. Lett.* **3**, 27–29 (1978).
48. Fienup, J. Iterative Method Applied To Image Reconstruction And To Computer-Generated Holograms. *Opt. Eng.* **19**, 297–305 (1980).
49. Bates, R. Uniqueness of solutions to two-dimensional fourier phase problems for localized and positive images. *Comput. Vis. Graph. Image Process* **25**, 205–217 (1984).
50. Miao, J., Kirz, J. & Sayre, D. The oversampling phasing method. *Acta Crystallogr. Sect. D Biol. Crystallogr.* **56**, 1312–1315 (2000).
51. Gerchberg, R. A practical algorithm for the determination of phase from image and diffraction plane pictures. *Optik* **35**, 237–246 (1972).
52. Bauschke, H., Combettes, P. & Luke, D. Phase retrieval, error reduction algorithm, and Fienup variants: a view from convex optimization. *J. Opt. Soc. Am. A* **19**, 1334–1345 (2002).
53. Fienup, J. Phase retrieval algorithms: a comparison. *Appl. Opt.* **21**, 2758–2769 (1982).
54. Fienup, J. Reconstruction of a complex-valued object from the modulus of its Fourier transform using a support constraint. *J. Opt. Soc. Am. A* **4**, 118–123 (1987).
55. Marchesini, S. Invited Article: A unified evaluation of iterative projection algorithms for phase retrieval. *Rev. Sci. Instrum.* **78**, 011301 (2007).
56. Wu, L., Juhas, P., Yoo, S. & Robinson, I. Complex imaging of phase domains by deep neural networks. *IUCrJ* **8**, 12–21 (2021).
57. Cherukara, M. et al. Three-dimensional X-ray diffraction imaging of dislocations in polycrystalline metals under tensile loading. *Nat. Commun.* **9**, 3776 (2018).
58. Yao, Y. et al. AutoPhaseNN: unsupervised physics-aware deep learning of 3D nanoscale Bragg coherent diffraction imaging. *Npj Comput. Mater.* **8**, 1–8 (2022).
59. Nguyen, T., Xue, Y., Li, Y., Tian, L. & Nehmetallah, G. Deep learning approach for Fourier ptychography microscopy. *Opt. Express* **26**, 26470–26484 (2018).
60. Ronneberger, O., Fischer, P. & Brox, T. U-Net: Convolutional Networks for Biomedical Image Segmentation. *Med. Image Comput. Comput. Assist. Interv.* **9351**, 234–241 (2015).
61. Robinson, I., Vartanyants, I., Williams, G., Pfeifer, M. & Pitney, J. Reconstruction of the Shapes of Gold Nanocrystals Using Coherent X-Ray Diffraction. *Phys. Rev. Lett.* **87**, 195505 (2001).
62. Marchesini, S. et al. X-ray image reconstruction from a diffraction pattern alone. *Phys. Rev. B* **68**, 140101 (2003).
63. Huang, X. et al. Incorrect support and missing center tolerances of phasing algorithms. *Opt. Express* **18**, 26441–26449 (2010).
64. Kingma, D. & Ba, J. Adam: A Method for Stochastic Optimization. *CoRR* **1412**, 6980 (2014).
65. Newton, M., Nishino, Y. & Robinson, I. Bonsu: the interactive phase retrieval suite. *J. Appl. Crystallogr.* **45**, 840–843 (2012).
66. Momma, K. & Izumi, F. VESTA3 for three-dimensional visualization of crystal, volumetric and morphology data. *J. Appl. Crystallogr.* **44**, 1272–1276 (2011).

Acknowledgements

This work was supported by UK Research and Innovation (UKRI) grant MR/T019638/1 for the University of Southampton Department of Physics & Astronomy. The authors acknowledge the use of the IRIDIS High-Performance Computing Facility, and associated support services at the University of Southampton, in the completion of this work. We acknowledge Diamond Light Source for time on Beamline I16 under Proposal MM25437-2.

Author contributions

A.H.M. synthesised the nanocrystals. M.C.N. designed and supervised the project. A.H.M. and M.C.N. performed the reconstructions and data analysis. All authors contributed to the BCDI experiment. A.H.M. wrote the manuscript with inputs from all authors.

Competing interests

The authors declare no competing interests.

Additional information

Supplementary information The online version contains supplementary material available at <https://doi.org/10.1038/s41524-024-01287-6>.

Correspondence and requests for materials should be addressed to Ahmed H. Mokhtar or Marcus C. Newton.

Reprints and permissions information is available at <http://www.nature.com/reprints>

Publisher's note Springer Nature remains neutral with regard to jurisdictional claims in published maps and institutional affiliations.

Open Access This article is licensed under a Creative Commons Attribution 4.0 International License, which permits use, sharing, adaptation, distribution and reproduction in any medium or format, as long as you give appropriate credit to the original author(s) and the source, provide a link to the Creative Commons licence, and indicate if changes were made. The images or other third party material in this article are included in the article's Creative Commons licence, unless indicated otherwise in a credit line to the material. If material is not included in the article's Creative Commons licence and your intended use is not permitted by statutory regulation or exceeds the permitted use, you will need to obtain permission directly from the copyright holder. To view a copy of this licence, visit <http://creativecommons.org/licenses/by/4.0/>.

© The Author(s) 2024